REPORT DOCUMENTATION PAGE

Form Approved
OMB NO. 0704-0188

Public Reporting burden for this collection of information is estimated to average 1 hour per response, including the time for reviewing instructions, searching existing data sources, gathering and maintaining the data needed, and completing and reviewing the collection of information. Send comment regarding this burden estimates or any other aspect of this collection of information, including suggestions for reducing this burden, to Washington Headquarters Services, Directorate for information Operations and Reports, 1215 Jefferson Davis Highway, Suite 1204, Arlington, VA 22202-4302, and to the Office of Management and Budget, Paperwork Reduction Project (0704-0188,) Washington, DC 20503.

1. AGENCY USE ONLY (Leave Blank)	2. REPORT DATE 11/17/2005	3. REPORT TYPE AND DATES COVERED Final Report (8/03-11/05)

4. TITLE AND SUBTITLE
Snapshot-Imaging Spectrpolarimeter

5. FUNDING NUMBERS
C: DAAD19-03-1-0276

6. AUTHOR(S)
Nathan Hagen & Eustace L Dereniak

7. PERFORMING ORGANIZATION NAME(S) AND ADDRESS(ES)
University of Arizona
College of Optical Sciences
1630 E. University Blvd.
Tucson, AZ 85721

8. PERFORMING ORGANIZATION REPORT NUMBER
IR1

9. SPONSORING / MONITORING AGENCY NAME(S) AND ADDRESS(ES)
U. S. Army Research Office
P.O. Box 12211
Research Triangle Park, NC 27709-2211

10. SPONSORING / MONITORING AGENCY REPORT NUMBER
44522.1-PH

11. SUPPLEMENTARY NOTES
The views, opinions and/or findings contained in this report are those of the author(s) and should not be construed as an official Department of the Army position, policy or decision, unless so designated by other documentation.

12 a. DISTRIBUTION / AVAILABILITY STATEMENT
Approved for public release; distribution unlimited.

12 b. DISTRIBUTION CODE

13. ABSTRACT (Maximum 200 words)

We have constructed a snapshot imaging spectropolarimeter for use in the visible spectrum, ultimately with the aim of obtaining imaging measurements of dynamic stress across a transparent material. After constructing the instrument, we found that a new calibration methodology was necessary in order to retain sufficient spectral resolution. Modifying the calibration enabled the instrument to obtain useful measurements, but the utility of the instrument is still severely hampered by the limitations of its design and its sensitivity to noise. This led to study of how the instrument design can be modified to optimize its performance, and how the reconstruction algorithms can be modified to improve their accuracy in the presence of noise.

14. SUBJECT TERMS
spectropolarimeter, imaging spectrometer, hyperspetral imaging

15. NUMBER OF PAGES
16

16. PRICE CODE

SNAPSHOT IMAGING SPECTROPOLARIMETER

Nathan Hagen, Eustace L. Dereniak

Optical Sciences Center, University of Arizona, Tucson, AZ 85721

1. INTRODUCTION

Digital cameras are used everywhere for the remote detection of objects. However, their limited color discrimination (typically limited to black-and-white, or to the three color bands RGB) means that many different objects can appear the same. An imaging spectrometer detects the spectrum of the object at higher resolution, improving our knowledge of the object composition. Polarization is another quantity which can tell us more about the object under view (*i.e.* its roughness, the angle of its surface relative to the viewing angle, etc.) As we add in all of the additional quantities into our measurement of an object, however, we find that the measurements themselves begin to take a lot of time. If the object is moving while the measurement is being taken, or if it is changing physically, artifacts occur in the data which degrade the measurement. Our research aim is to build a device which can measure the spatial, spectral, and polarization information of a scene in a single snapshot in order to minimize temporal artifacts.

The data acquired by an imaging spectropolarimeter can be interpreted as an image of a four-dimensional volume, since a measure of radiance is obtained for four independent variables or indices: two spatial variables (x, y), wavelength (λ), and the Stokes vector index (j). We refer to this four-dimensional volume as the spectropolarimetric hypercube, illustrated in Fig. 1.

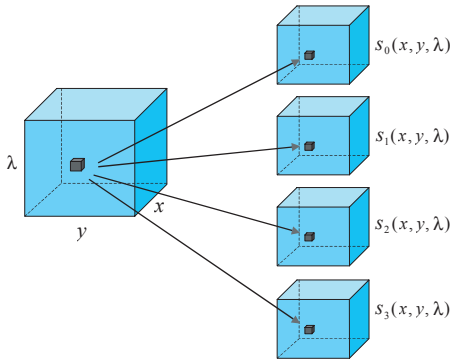

Figure 1. An illustration of the four-dimensional (x, y, λ, j) nature of the data acquired by an imaging spectropolarimeter.

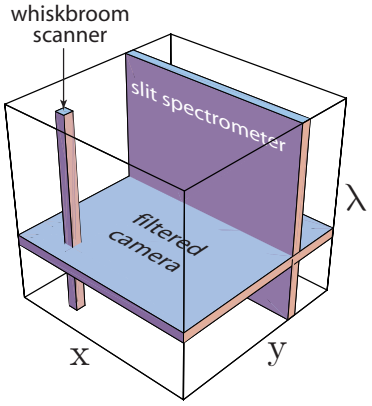

Figure 2. The lower-dimensional volumes which various spectrometer types are capable of imaging without scanning. Such spectrometers could be used with scanning to obtain spectral and spatial data on the s_0 polarization component, with additional measures (such as rotation of polarizers and retarders) necessary to obtain complete polarimetric data.

Conventional spectrometers and polarimeters are inherently sensitive to a one-, two-, or three-dimensional subset of the volume, and must scan out the remaining dimensions in order to obtain a complete data set. For example, a camera with a narrow-band filter could be used to obtain a single x,y slice through the hypercube. In this slice x and y vary while λ is fixed at the wavenumber passed by the filter and j is held at zero. The entire four dimensions could be swept out by swapping in filters with different transmission wavelengths in tandem with an analyzer and a rotating retarder. Similar examples can be made for other systems, such as slit spectrometers and whisk broom scanners (see Fig. 2).

Whereas imaging spectrometers are widely used in remote sensing applications (Earth-observing satellites such as AVIRIS are well-known examples), imaging spectropolarimeters are uncommon, largely due to the hardware difficulties introduced by adding polarimetry to an instrument. Traditional approaches use moving parts, which reduce reliability and robustness, and that a relatively long time is required for the capture of a complete data set, since multiple exposures are made sequentially in time. Past efforts to build snapshot instruments have faced extreme difficulties in integrating large complex optical systems with multiple focal plane arrays. We hope to show a method which can accomplish this with a compact optical system, relying more on computational complexity than hardware complexity.

2. BACKGROUND — COMPUTED TOMOGRAPHY IMAGING SPECTROMETRY (CTIS)

The CTIS design involves imaging through a 2D transmission grating, with the result that the imaged scene is dispersed into a rectangular array of prismatic images (Fig. 6).[1,2] The grating (or "disperser") is placed into the collimated path in front of the focal plane array (in this case a CCD camera). By placing a field stop at a conjugate plane to the FPA, we can limit the spatial extent of the scene imaged, allowing the prismatic images to be spatially separated (Fig. 4).

The grating is a computer generated hologram, generated as a 2D rectangular surface relief pattern fabricated from PMMA (plastic).[3,4] The grating is designed to produce the desired dispersion pattern for the spectral range of the instrument, which for the prototype instrument used here is the visible spectral region (400 nm–700 nm).

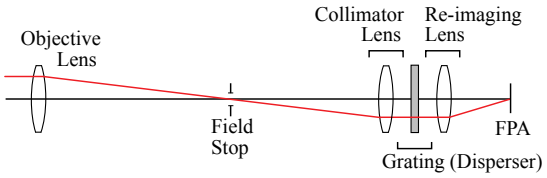

Figure 3. The CTIS optical layout.

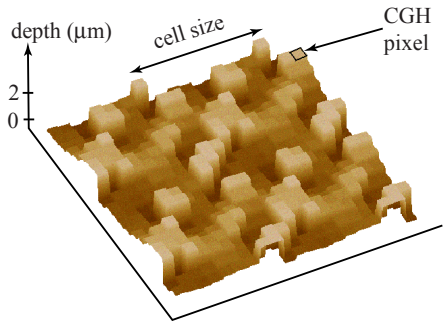

Figure 4. The surface relief pattern of the 2D grating ("disperser"). Shown here is a section of the grating (2 cells × 2 cells), where each cell comprises 10×10 "phasels".

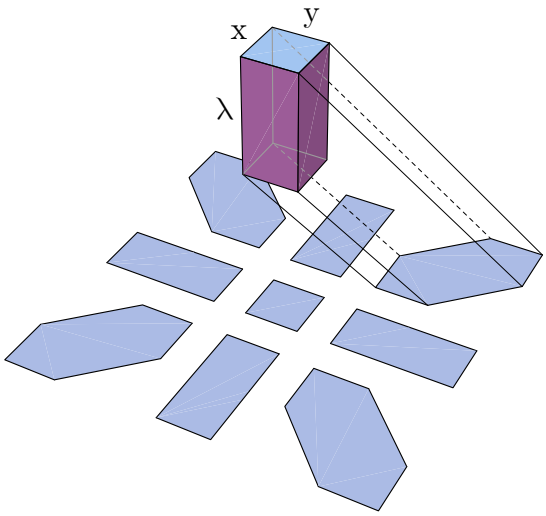

Figure 5. A typical image from a CTIS FPA, shown with the computed-tomographic model of projections of the data cube onto the FPA.

The prototype system we have constructed uses a 2048 × 2048 pixel B/W CCD camera, and the grating has been designed to produce what we call a 5 × 5 CTIS diffraction pattern (the measured diffraction orders are $+2, +1, 0, -1$, and -2, for a total of 5 measured orders in each of the horizontal and vertical directions). The undiffracted (zero-order) image in the center of the FPA is basically a miniature black-and-white imager which provides the spatial resolution of the datacube. The prototype system we have constructed currently provides a zero-order image size of 70 × 70 pixels. The best spectral sampling of the object is provided by the outer

diffraction orders, where the spectral projection is the most spread out. Here, the outer diffraction orders in the prototype system are smeared (spatially and spectrally multiplexed) across a range of 600 pixels. Removing the spatial component (100 pixels along the diagonal), gives the maximum spectral sampling achievable by this setup: 500 spectral bands in the visible region.

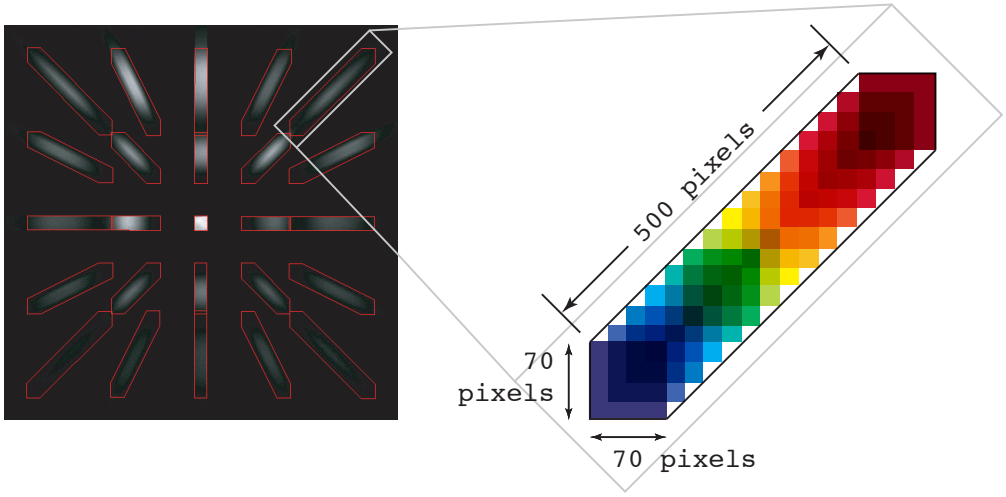

Figure 6. A raw CTIS image (with outlines of each diffracted order superimposed). The blowup of the corner diffracted order gives a figurative illustration of the spatial and spectral multiplexing.

To develop a method for reconstructing the dispersed prismatic images into a single datacube, we can start with the linear imaging equation[5]

$$\underset{\substack{\text{image}\\(\text{output})}}{\mathbf{g}} = \underset{\substack{\text{system}\\\text{operator}}}{\mathbf{H}} \quad \underset{\substack{\text{object}\\(\text{input})}}{\mathbf{f}(x, y, \lambda)}$$

If we lexicographically order the pixel information of our detected image $\mathbf{g}$ into a long 1D vector (indexed by i) and do the same for each voxel in the datacube $\mathbf{f}$ (indexed by j), then each column H_i of the system matrix H maps a single voxel in the datacube to a set of pixels in the image. The system H-matrix can then be calibrated (that is, its elements can be determined) by using a series of detected images $\mathbf{g}$ of a quasi-monochromatic point-source $\mathbf{f}$: by placing a single-mode optical fiber directly into the field stop and illuminating it with a monochromator, we effectively have a source which is contained inside a single voxel of the datacube. Adjusting the wavelength then allows us to map out a full vertical column of voxels in the datacube.

$$\boxed{g_i = H_{ij}\, f_j}$$
discrete imaging equation

Then, for *unknown* inputs f, the calibration can be used to construct estimates $\hat{f}$ of the datacube representing the input:

$$\boxed{\hat{f}_j = H^{+}_{ji}\, g_i}\,,$$
calibrated measurement

where H^{+} is the Moore-Penrose pseudoinverse of the calibrated system matrix. From the method used to calibrate the system matrix H we can get an idea of what kind of operation its pseudoinverse H^{+} performs. The values of the individual matrix elements in H are the weights in the mapping of datacube voxels to FPA pixels: an element with a large value means that a large amount of the energy from a given voxel gets imaged onto the pixel to which it is mapped. We can now imagine what it means to do this in reverse: given a set of

intensities measured on the FPA, we can then use these measured weights to backproject the pixel intensities into the voxels in the datacube to which they are mapped. (Each pixel will get mapped to multiple voxels because of the spectral-spatial multiplexing of the system.) This backprojection process causes blurring, since by itself it can't de-multiplex the spatial from the spectral components, so the backprojection is followed by a filtering operation that reduces the blurring artifacts. In rough form, this backprojection+filtering is the process that the pseudoinverse matrix represents for this system.

3. CHANNELLED SPECTROPOLARIMETRY (CHSP)

Channelled spectropolarimetry[6] is a technique which, through the simple addition of a pair of thick retarders and an analyzer to an optical system, allows the conversion of a spectrometer into a spectropolarimeter, and therefore also an imaging spectrometer into an imaging spectropolarimeter. Its great advantages include its compactness and its lack of moving parts.

CHSP uses the dispersion of birefringence in high-order retarders to interfere components of the input beam. For example, we can consider a spectrum which is passed through a horizontal polarizer, after which it is incident on a thick retarder oriented at 45°(see Fig. 7). To consider what happens to the light as it passes through the retarder, we split it into two equal components — the projections onto the +45° and −45° axes of the retarder. When the light emerges from the retarder, these two components (+45° and −45°) will be out of phase by an amount given by the retardance of the waveplate. For simple waveplates, the retardance varies linearly with wavenumber $\sigma := 1/\lambda$:

$$\delta(\sigma) = 2\pi d\,\Delta n\,\sigma \ ,$$

where d is the physical thickness of the retarder. (This nice linear relationship assumes a waveplate material which has a low dispersion of birefringence.) Thus, the blue end of the spectrum will see a large retardation between the +45° and −45° components, while the red end of the spectrum will see much less retardation. If a horizontally-aligned analyzer is then placed into the beam, the two components (+45° and −45°) are forced to interfere, and since there is a linear phase ramp going from the blue to red wavelengths, the spectrum is modulated (at a frequency given by the retardance).

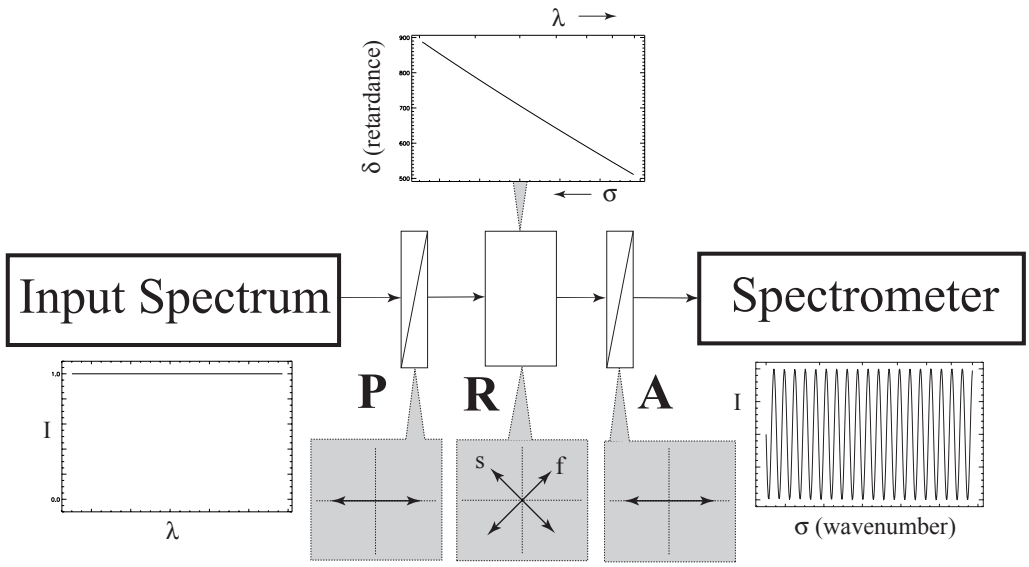

Figure 7. When a horizontally-polarized spectrum is passed through a high-order retarder oriented at 45°, and then passed through a horizontally-oriented analyzer, the spectrum is modulated at a constant frequency.

To build a complete polarimeter with this technique, it is necessary to produce interference not only in the horizontal/vertical linear polarization components [⇿] of the beam but also the +45°/−45° linear components [⤫]

and the circular components (RCP/LCP) [8]. Fig. 8 illustrates the principle of operation: the input broadband spectrum passes through two high-order retarders; the first retarder is aligned with the analyzer's transmission axis and the second retarder is aligned at 45°to the first. Using Mueller calculus, and representing the spectrum in terms of wavenumber σ rather than λ, we can relate the measured spectrum $I(\sigma)$ in terms of the Stokes vector polarization components in the input beam

$$2I(\sigma) = s_0 + s_1\cos(\delta_2) + s_2\sin(\delta_1)\sin(\delta_2) - s_3\cos(\delta_1)\sin(\delta_2)\ ,$$

where δ_1 and δ_2 are the retardances of the respective retarders (and each are linear functions of wavenumber σ). Taking the autocorrelation of $I(\sigma)$, we obtain a function in which the four individual Stokes components are separated into seven channels (the seven terms of equation (3)). By proper choice of thicknesses for the two retarders,[7] which decide the retardances δ_1 and δ_2, these channels do not overlap, so that windowing each channel individually and taking the forward Fourier transform of the result, we have the four spectrally-resolved Stokes components. Because the individual channels occupy only a portion of the total signal bandwidth, there is a reduction in overall spectral resolution (by a factor of seven, typically) in the reconstructed Stokes spectra.

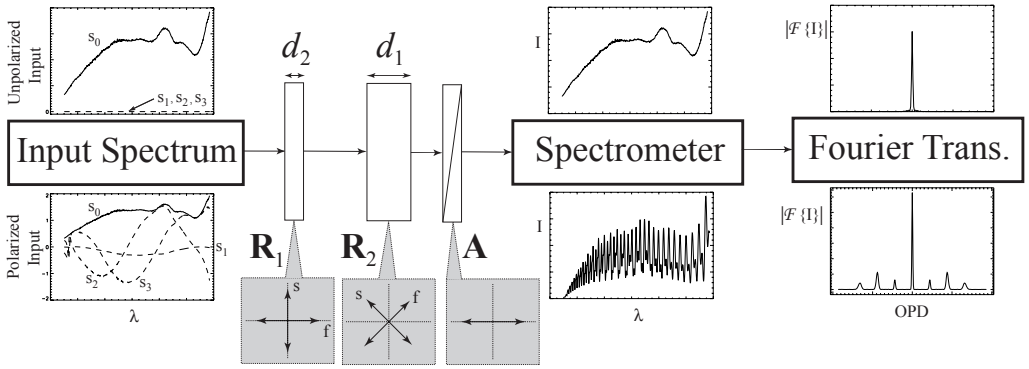

Figure 8. Channelled spectropolarimeter diagram (adapted from ref. 6). The input spectrum passes through a thick retarder oriented at 0°to the horizontal, then another thick retarder oriented at 45°, followed by an analyzer at 0°and a spectrometer. An unpolarized input spectrum is unmodulated, while a polarized input is given high-frequency modulations. In the Fourier domain, the polarization components of the beam are (with a proper choice of retarder thicknesses) separated into 7 channels. The s_j terms shown here are the Stokes vector components representing the polarization state.

If we pass a polarized spectrum into a CHSP instrument, we see that the spectrum is given high-frequency modulations (Fig. 9). If we now calculate the Inverse Fourier Transform of this spectrum, $C(\mathrm{OPD}) = \mathcal{F}^{-1}\{I(\sigma)\}$, we can see the resulting 7-channel distribution in the Fourier domain. The Stokes component terms are separated into independent channels, much in the way that communications systems using a single carrier frequency reserve bandwidth regions for each independent communication channel, referred to as *sideband modulation*.

As long as none of the Stokes component spectra $s_j(\sigma)$ exceed the bandwidth of a given channel, then each of the Stokes components can be extracted separately via masking and shifting in the Fourier domain. The spectral resolution of the system may then be characterized by the OPD-bandwidth provided to each channel. For quartz retarders, the birefringence at visible wavelengths is approximately 1% of the crystal's physical thickness, so that for the pair of quartz retarders used to generate the data in the figures here, with thicknesses of 1.84 and 5.52 mm respectively, there is a retardance of $\delta_1 \approx 18.4\ \mu$m for the orthogonal polarizations passing through the thinner retarder. This gives the width of each individual channel shown in Fig. 9.[8]

4. SNAPSHOT IMAGING SPECTROPOLARIMETRY (CTICS)

By combining the techniques of CTIS with CHSP, we can construct an instrument which maintains snapshot capability and obtains information of the four-dimensional hypercube (Fig. 1). Fusing the two techniques involves the insertion of the pair of high-order retarders and analyzer into the collimated path in front of the CTIS

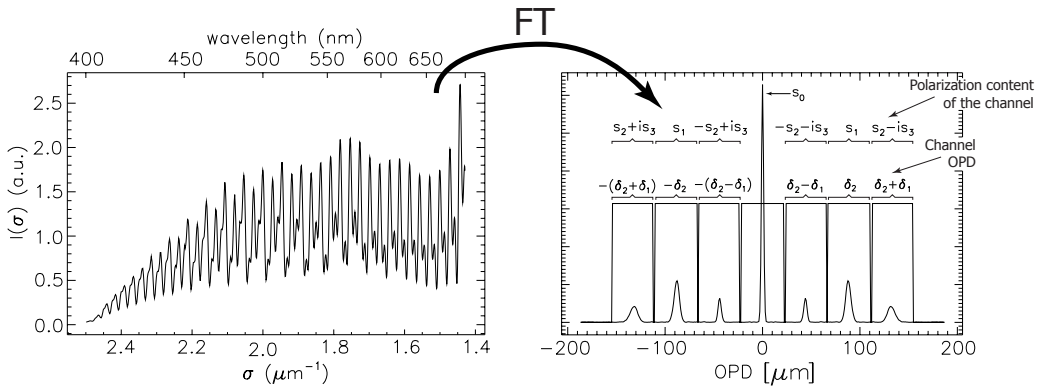

Figure 9. (Left:) The measured channelled spectrum for a compound input polarization state. (Right:) The magnitude of the spectrum's Fourier Transform $|C(\mathrm{OPD}|)$ for the input polarization state. Windows have been superimposed onto the plot to show the seven channels and the bandwidth region into which each polarization component of the input spectrum is distributed.

disperser, so that the polarization information in the measured scene can now be encoded in modulations in the spectrum. This additional capability comes at the cost of reducing the spectral resolution by a factor of 7, but snapshot capability is maintained.

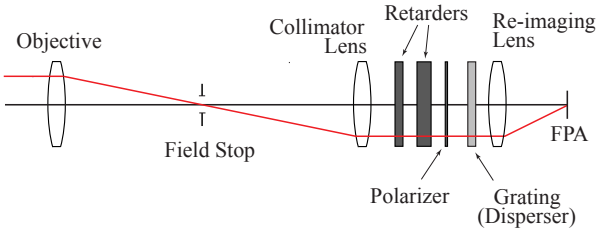

Figure 10. The layout of the CTICS system, with the pair of high-order retarders and analyzer inserted in front of the disperser.

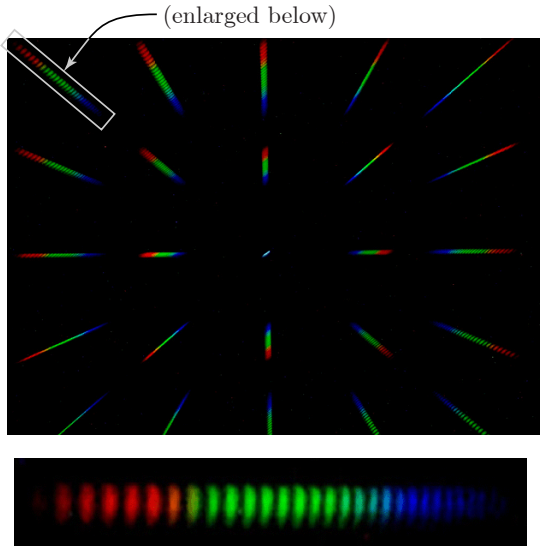

Figure 11. If we image horizontally-polarized light through a narrow slit, we can see the channelled spectrum most easily in the diffraction order oriented perpendicularly to the slit.

The addition of the polarization components into the system significantly affects the calibration methods, however. As mentioned above, the CTIS calibration involves placing a monochromatic point-source into the field stop (a conjugate plane to the image) and measuring the response of each pixel in the image to each voxel of the datacube. With the CHSP hardware installed, we follow this procedure as before, making sure that the point-source used is unpolarized. This allows us to reconstruct the s_0 datacube. In order to obtain the remaining three components of the hypercube, we then calibrate the retardances of each of the two thick retarders and use those values to demodulate the spectrum (a column of the data cube) via the Fourier windowing technique for

each channel.

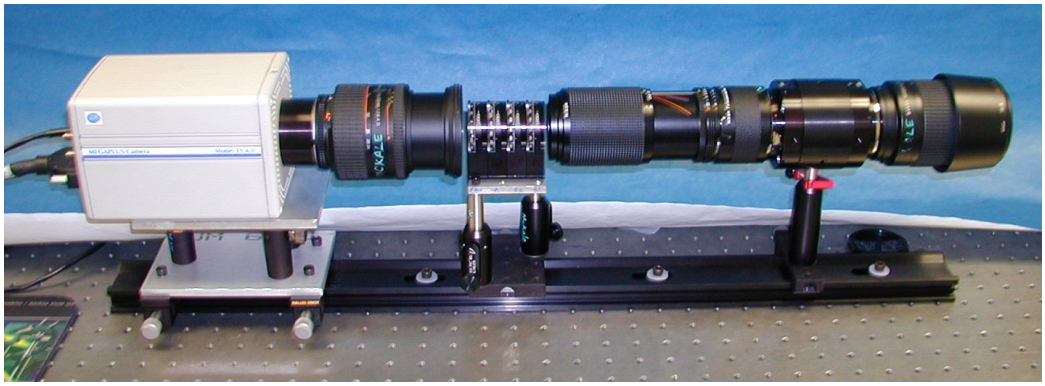

Figure 12. The prototype visible-spectrum CTICS instrument. The physical length of the entire instrument is about 75 cm.

5. IMPLEMENTATION

After integrating the CTICS system shown in Fig. 12, we made our first attempts at calibration and soon learned that the monochromator available in the lab does not have sufficient light output to allow a narrow band spectral spectral output for our calibration. If the spectral band is narrowed to the width of the resolution of our CTICS system (1 nm FWHM), the light output is feeble and the calibration images become swamped with noise. If the spectral band is widened to allow enough signal through, the system's spectral resolution suffers — rather than mapping one datacube voxel to a set of FPA pixels, a wideband calibration input maps a set of voxels to a large set of pixels, which will result in substantial blurring in the reconstruction. To compensate for these effects, we first designed a new mounting system (mentioned above) which allows us to place the tip of a single-mode fiber directly into the field stop (the standard CTIS calibration method has been to *image* the tip of the fiber into the field stop, which results in large signal loss and in chromatic aberration). While this gave a large increase in signal, the increase was still not enough to allow us to narrow the monochromator output down to the needed 1 nm FWHM.

To modify the CTIS calibration to maximize spectral resolution, the approach we take is as follows. Increasing the spectral width of the monochromator output provides enough light, but the resulting image of the point-source becomes a streak rather than something pointlike (as shown in the left hand side image of Fig. 13). A CTIS calibration image thus will contain 25 streaks rather than 25 points. If we use a Gaussian fitting routine to locate the center of each streak, we can effectively locate the central wavelength of the monochromator output. This works because the monochromator's output $I(\lambda)$ is basically symmetric about the center wavelength. At the same time, we can see that diffraction increases the size of the PSF only along the diffraction direction; orthogonal to the diffraction direction, the shape of the streak is purely due to the PSF itself. This gives a clue about how to estimate the PSF for a given wavelength: we can sum pixels along the diffraction direction, leaving only the 1D projection of the PSF along a direction orthogonal to the diffraction angle (this is shown in Fig. 14). We have 25 projections in a 5×5 CTIS design, but some of the projection angles coincide, so that there are actually a total of only 8 non-redundant projection angles available. We can use tomographic methods to try to reconstruct the 2D PSF from these projections, but we currently assume rotational symmetry so that each of the projection angles can be treated as being estimates of the 1D PSF expressed in polar form. The final step is then to interpolate this radial PSF onto the pixel grid at the location of the center wavelength. The resulting processed data is shown in Fig. 13 below.

As far as the system **H**-matrix is concerned, the difference between using the raw calibration images (where the point-source images take the form of short streaks) and the processed calibration images (where the point-source images are copies of the PSF) is that less data smoothing takes place during the reconstruction step. To

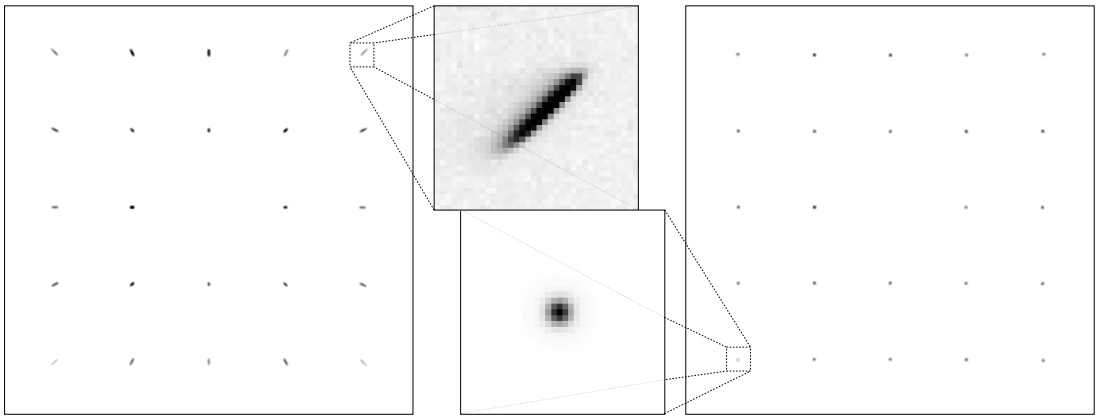

Figure 13. (**Left**:) A *raw* CTIS calibration image using a monochromator with substantial spectral width (∼5 nm FWHM). (**Right**:) A *processed* CTIS calibration image, where the system PSF has been interpolated onto the position of the raw image's centroid. The processed image is therefore equivalent to an image of an ideal monochromatic point-source. The features in both images have been enlarged to enhance visibility.

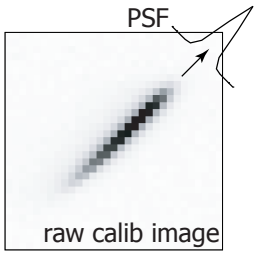

Figure 14. The image of the calibration pointsource taken from the upper-right corner diffraction order. Projecting the image along the diffraction direction provides a 1D tomographic projection of the PSF.

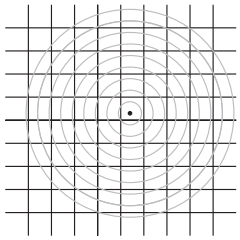

Figure 15. After obtaining an estimate of the PSF, we interpolate the circularly-symmetric PSF onto the rectangular position grid, at a point centered around the measured centroid of the original calibration streak.

make the distinction clear, we can use the notation $\mathbf{H}_{\text{raw}}$ and $\mathbf{H}_{\text{psf}}$ to describe the system matrices resulting from the two respective methods.

During the measurement step, where we attempt to estimate the datacube from a given image, the reconstruction algorithms attempt to de-multiplex and deblur the spatial and spectral components of the data. Using the original and modified calibration techniques described above, we have reconstructed the spectropolarimetric hypercube for a broadband polarized source. The channelled spectrum at a given spatial location in the cube, and the resulting reconstructed Stokes spectra, are shown in Figs 16 & 17. The effect of additional blurring on the spectrum reconstructed from $\mathbf{H}_{\text{raw}}$ is apparent, indicating that the modified calibration method has succeeded in improving the realizable spectral resolution of the system.

Although the new calibration approach shows some success, artifacts in the reconstructed data show that work is still needed to bring the system up to a standard where it can make useful scientific measurements. The figures were taken for a pointsource object, which minimizes the blurring taking place in the CTIS reconstructions, and at a polarization of 45°, which produces the lowest-frequency modulations. For such a well-behaved object, the reconstruction is marginally useful, but for a more realistic scene the reconstruction is severely limited in usefulness. Thus, further work is needed, and the next couple sections outline our work in trying to find new CTIS designs that can overcome current limitations, and we are starting to work on modifying existing reconstruction algorithms to reduce noise amplification.

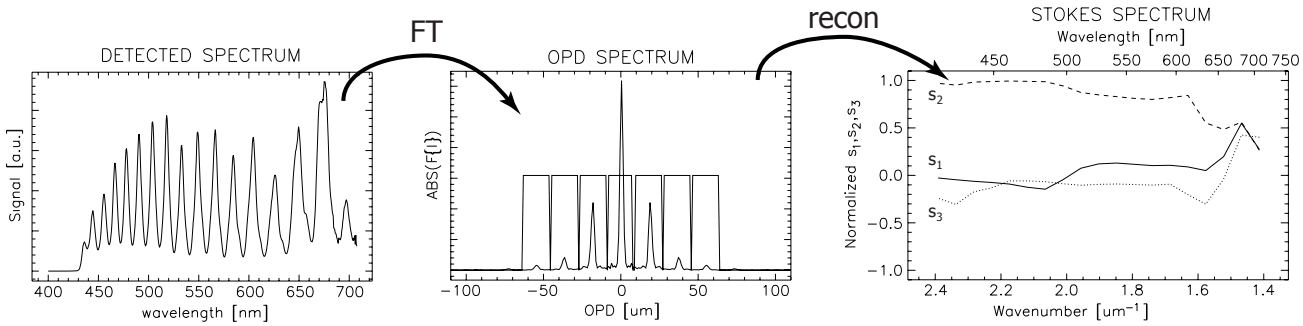

Figure 16. Using a 45°linearly polarized source imaged by the CTICS, the above figures show: (*i*) the spectrum obtained from a column of a datacube reconstructed with $\mathbf{H}_{\text{raw}}$, (*ii*) its Fourier-domain representation (the Fourier windows are shown superimposed), and (*iii*) the reconstructed Stokes spectra for this location in the object. The noise in the reconstructed polarization state, especially at the longer wavelengths, indicates the unreliability of the measurement.

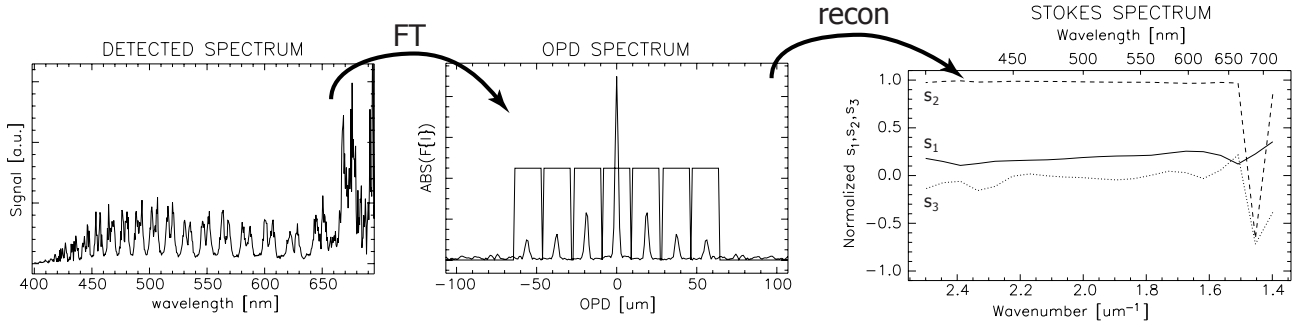

Figure 17. Using the same source as in Fig. 16, the figures here show the same measurements, obtained this time with $\mathbf{H}_{\text{psf}}$. The improved preservation of higher frequencies is apparent, which also provides an improved measurement of the Stokes spectra, but the presence of substantial noise is still apparent.

6. CTIS DESIGN IDEAS: "A MENAGERIE OF CTISES"

For a long time, the evolution of CTIS designs has been to increase the number of diffraction orders. The original CTIS design employed three crossed cosine gratings — gratings designed to produce diffraction only in the orders $+1$ and -1. The next CTIS design (the "5×5" design) used a CGH to generate a diffraction pattern using the $+2, +1, 0, -1$ and $+1$ orders in the vertical and horizontal directions. A later design (the "7×7") took a step further and superimposed a total of 49 spectral footprints onto the focal plane array, generated by taking the $+3$ through -3 diffraction orders for both vertical and horizontal directions.

Looking at past work on these CTIS designs, however, we realized that to produce good reconstructed datacubes it should be sufficient to use only the $+1$ and -1 diffraction orders, if we then change the diffraction pattern to increase the number of projections. This would give a pattern something like the one shown in Fig. 19.

Another issue that needs to be addressed in considering new CTIS designs is that of the special requirements for integrating polarimetry into the system — very high spectral resolution. Current CTIS disperser designs are severely limited in the spectral dispersion they can produce just by the fact that the dispersion angle is linear in wavelength. If, for example, we design 700 nm light to get dispersed to the edge of the array, then 400 nm light is necessarily diffracted by 4/7ths of that angle (as in Fig. 20). The space between the zero-order light and the low-wavelength image is then completely empty (if the field stop is small enough, you can actually fit an entire inner diffraction order inside that "optimized" diffraction design). If possible, it would help the spectral resolution greatly if we could modify the grating design to achieve *nonlinear* dispersion angle with wavelength.

Thus, a good CTIS design will maximize the use of space on the focal plane array to optimize spatial and spectral resolution while maintaining as many independent projections as possible. An early idea was to try a dispersion pattern which is rotationally symmetric (what may be called a "conical" grating design due to the

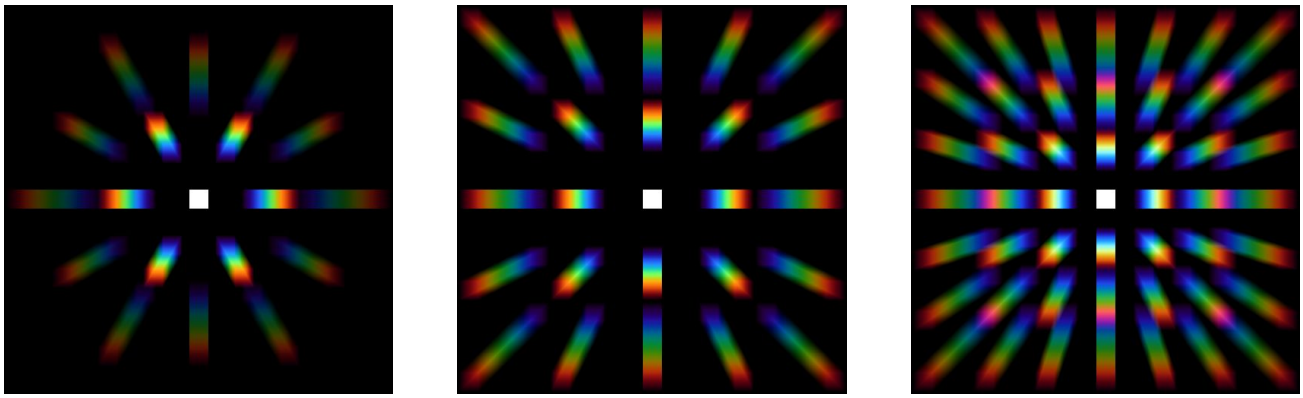

Figure 18. Past CTIS grating designs. (Left:) The CTIS pattern on the FPA produced by three crossed cosine gratings. (Center:) The CTIS pattern produced by the 5×5 design. (Right:) The CTIS pattern for the 7×7 design.

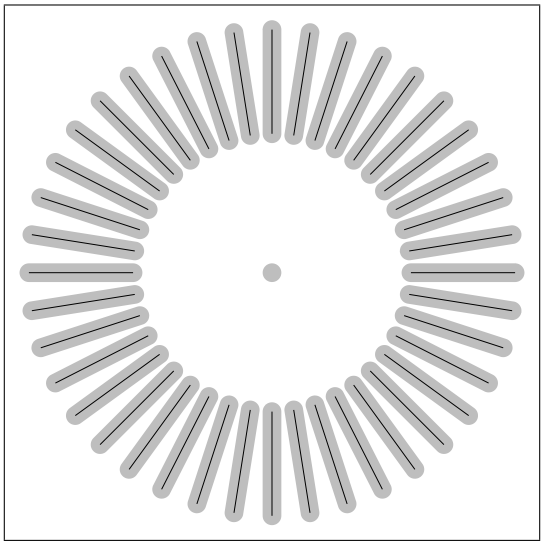

Figure 19. The CTIS footprint for a design using a radial spoke pattern and a circular field stop.

shape of the wavefront exiting the grating, as shown in Fig. 22). From a system-level perspective, such a grating would mean that a single voxel in the datacube would produce a *ring* of light on the array. We no longer have a discrete number of projections but rather a continuum of projections in all angles. If we look at a different voxel in the datacube, the ring of pixels on the detector array corresponding to that voxel are translated over. If the voxel illuminating the array is at a different wavelength then the radius of the ring changes. This is strongly reminiscent of the annulus aperture well-known from coded aperture imaging: there, the shape of the PSF is a ring whose center gives the angle towards the source, and whose magnification indicates the distance to the source.

However, the conical design possesses some serious drawbacks. The problems CTIS experiences in optimizing spatial and spectral resolution come primarily from the mixing between components. The system operator $\mathbf{H}$ is basically a blurring operator, and our reconstruction algorithms make the best attempt possible to recover the unblurred object. The more that blurring occurs in a given CTIS design, the more difficult the reconstruction is going to be (and, given noise considerations, the quality of the result will be lower). If we have more projections, then the multiplexing (or blurring) happens between different components of the signal, making it easier to reconstruct the underlying signal in the presence of noise. While the conical grating design has the nice property of allowing having every possible projection on a discrete rectangular array, the price to be paid is that the mixing is enormously increased, especially in the blue end of the spectrum. The result is likely a workable CTIS,

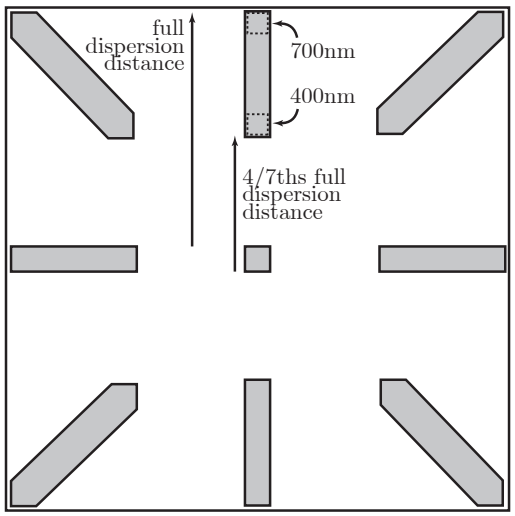

Figure 20. If the zero-order image is kept small in order to maximize spectral resolution, then the maximum achievable dispersion of a grating designed for linear dispersion, not matter what diffraction order, is shown above for the case of the visible spectrum range, 400 nm–700 nm. (If using a wide (multi-octave) spectral range, this dispersion can approach the nonlinear pattern shown below.

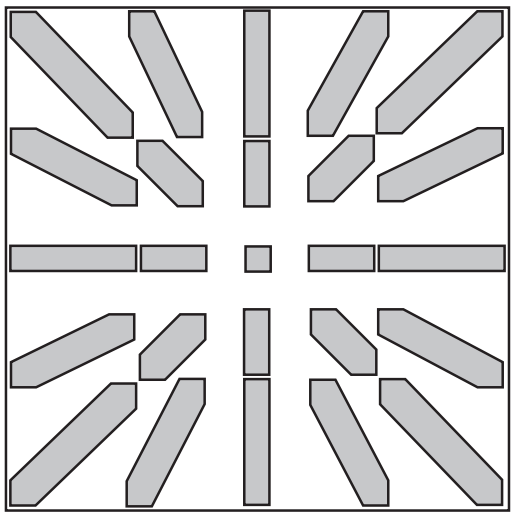

Figure 21. The current 5×5 dispersion CTIS design configuration, optimized for maximum spectral dispersion. For a visible-spectrum system, the inner diffraction orders fit entirely inside the outer diffraction orders, even when the outer orders are maximally dispersed.

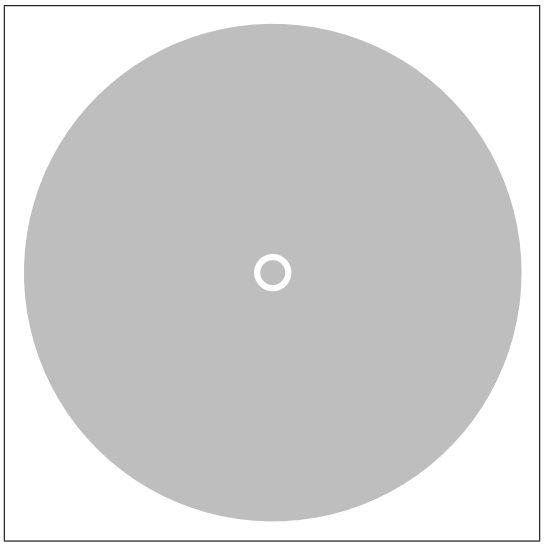

Figure 22. The *conical* CTIS design.

but hardly an optimized CTIS.

To compare some of the CTIS designs, we need to define some metrics which correspond to desired system parameters. Thus, we can define the number of projections produced by a given design, the maximum spectral resolution achievable, and the amount of blurring that occurs. (The maximum spectral resolution number is basically meaningless if all of the data is severely blurred together.)

To characterize the amount of blurring in a given design, we can define a *Blur Factor*, given by the number of voxels that the average illuminated pixel maps to. (This is intended to correspond closely to the idea of backprojection, since that step is the core of the reconstruction algorithm.) While this gives the Blur Factor an

intuitive interpretation, it unfortunately means that the result is calibration-dependent. So, we can assume that for the purposes of defining the Blur Factor in each design the calibration images will be taken at evenly spaced wavelength steps which on average place the resulting images one pixel apart.

A set of CTIS designs is shown below, together with the design parameters relevant to each. The spatial resolution (in number of pixels) is given by D, and the number of projections (ignoring the zero-order) is given by N, where we have assumed that the detector array used is 2048×2048 pixels in size. (This produces numbers for D which are of a convenient size.) The maximum theoretical spectral resolution achievable for a design is given by L (representing the number of samples of the visible spectral region, 400 nm–700 nm).

Generally, one of the first things commented on regarding the limitations of spectral resolution in a CTIS system is: why can't we move the zero order to a corner of the detector and read off only a quadrant of diffraction orders (thus allowing twice the spectral resolution)? While it is obvious that this provides for only a small number of diffraction orders, which makes the de-multiplexing task more difficult, the problem needs a more thorough treatment to be convincing. In Section 7 below, we show how these "asymmetric" CTIS designs produce a sampling of frequency space which is sparse — much of the Fourier cube is empty (unsampled). However, we know that the detected data is real-valued, and that the Fourier Transform of a real-valued object has Hermitic symmetry. In 1D, this means that, for example, $F(\xi) = F^*(-\xi)$: if you measure the function for all positive values of ξ, the negative values can be readily supplied. Thus, collecting data in the negative half-space is unnecessary. Applied to the case of CTIS, this means that, in principle at least, it is possible to measure the data in *one octant* of the datacube and from that data reconstruct the missing samples in the remaining seven octants. Actually putting this idea into implementation is part of our continuing research effort.

Tables 1&2 below summarize the complete set of designs were are considering for using with a CTIS instrument. The D, N, and L factors are the same as given before, except that in the tables they are given both in terms of the fraction of the focal plane array or (in parentheses) in terms of pixels on the default 2048×2048 array. The *fill* factor describes the fraction of pixels on the array that are illuminated, and the *blur* factor gives the average number of voxels mapped to a given illuminated pixel on the array. The parameters ϕ and γ refer to properties of the designs in Fourier space, where ϕ is the "missing cone angle" and γ is the fraction of the sampled frequency space which lies inside the missing cone. An explanation of the Fourier approach is given in detail in the following section.

In the tabulated data, it should be mentioned that since the spiral designs cannot be represented by a linear projection, the spatial-spectral footprints on the array cannot be represented as sampling a planar region in Fourier space. However, in order to make some kind of comparison with the other designs here, the spiral patterns are assumed to be represented as equivalent radial design patterns (*i.e.* a nonlinear radial pattern with the same number of projections and spectral resolution as the spiral design).

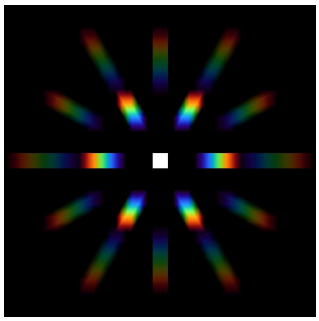

Figure 23. Descour design, $D = 100$, $N = 16$, $L = 550$.

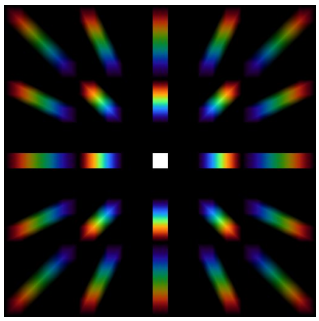

Figure 24. 5×5 design, $D = 100$, $N = 24$, $L = 526$.

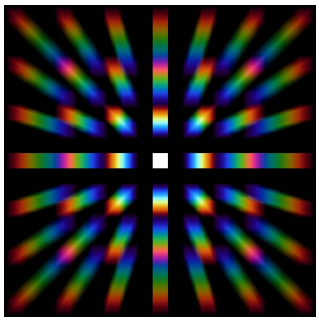

Figure 25. 7×7 design, $D = 100$, $N = 48$, $L = 526$.

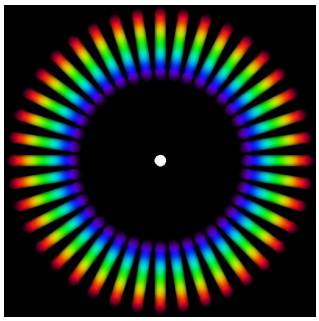

Figure 26. Linear radial design, $D = 75$, $N = 40$, $L = 419$.

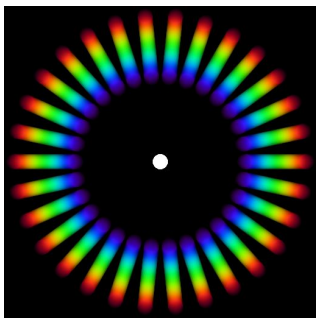

Figure 27. Linear radial design, $D = 100$, $N = 30$, $L = 413$.

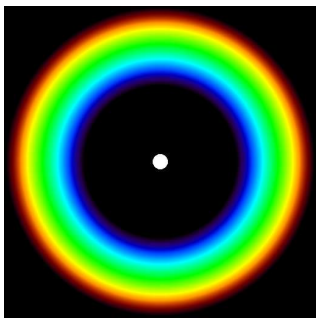

Figure 28. Linear conical design, $D = 100$, $N = \infty$, $L = 413$.

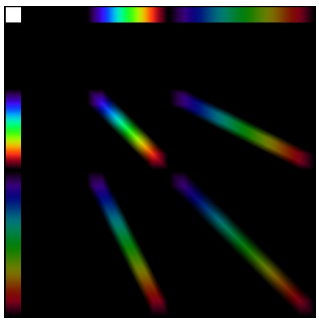

Figure 29. 5×5 corner design, $D = 100$, $N = 8$, $L = 1208$.

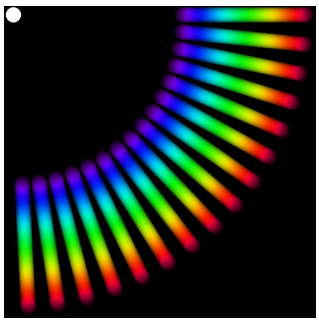

Figure 30. Linear radial corner design, $D = 100$, $N = 16$, $L = 826$.

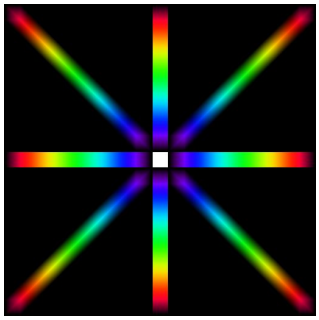

Figure 31. Nonlinear 3×3 design, $D = 100$, $N = 8$, $L = 1208$.

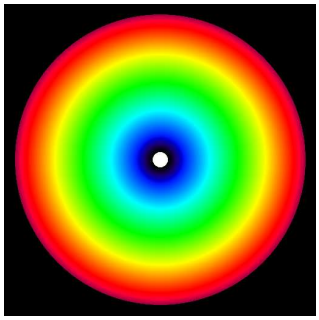

Figure 32. Nonlinear conical design, $D = 100$, $N = \infty$, $L = 854$.

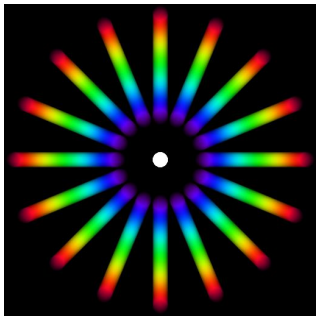

Figure 33. Nonlinear radial design, $D = 100$, $N = 16$, $L = 685$.

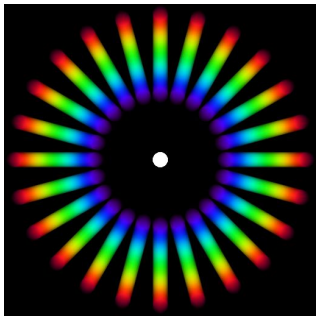

Figure 34. Nonlinear radial design, $D = 100$, $N = 24$, $L = 545$.

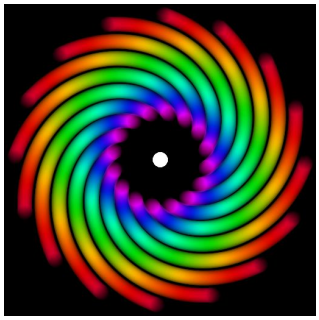

Figure 35. Spiral design, $D = 100$, $N = 16$, $L = 1501.13$

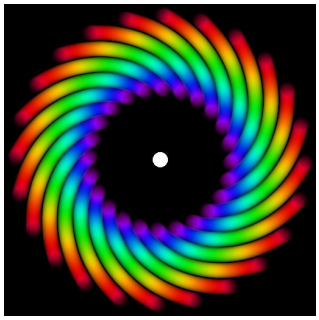

Figure 36. Spiral design, $D = 100$, $N = 24$, $L = 907$.

Table 1. *Comparison of the CTIS designs.* D = (dim of the zero order) / (dim of the full array), N = number of projections, L = (pixels of spectral dispersion) / (dim of the full array). Values in parentheses are for an array of dimension 2048 pixels. The linear designs have a Fourier cube scaled to $z = \pm 14.5$.

Design Parameters			Design Metrics					
Design Type	***D***	***N***	***L***	**Fill**	**Blur**	ϕ	γ	**Notes**
Linear Designs								
5x5 Full	0.03 (60)	24	0.29 (596)	0.19	67	5.78	0.058	
5x5 Outer	0.03 (60)	16	0.29 (596)	0.13	69	5.78	0.058	
Radial Linear	0.03 (60)	50	0.21 (422)	0.34	43	8.10	0.082	
Descour	0.04 (75)	18	0.27 (558)	0.18	111	7.66	0.089	
5x5 Full	0.04 (75)	24	0.28 (570)	0.24	81	7.50	0.099	(411nm – 700nm)
Radial Linear	0.04 (75)	40	0.20 (419)	0.35	53	10.16	0.146	
7x7 Linear	0.04 (75)	48	0.28 (570)	0.42	70	7.49	0.099	(411nm – 700nm)
Descour	0.05 (100)	18	0.27 (550)	0.25	141	10.28	0.163	
5x5 Full	0.05 (100)	24	0.26 (526)	0.31	102	10.76	0.206	(430nm – 700nm)
Radial Linear	0.05 (100)	30	0.20 (413)	0.37	68	13.60	0.265	
7x7 Full	0.05 (100)	48	0.26 (526)	0.54	112	10.76	0.206	(430nm – 700nm)
Descour	0.07 (150)	18	0.26 (536)	0.40	193	15.61		
Radial Linear	0.07 (150)	20	0.20 (402)	0.39	95	20.40		
5x5 Full	0.07 (150)	24	0.21 (438)	0.44	133	18.90		(469nm – 700nm)
7x7 Linear	0.07 (150)	48	0.21 (438)	$\sim$0.78	143	18.91		(469nm – 700nm)
Radial Linear	0.10 (200)	14	0.19 (391)	0.37	150	27.04		
Descour	0.10 (200)	18	0.25 (522)	0.57	236	20.95		
5x5 Full	0.10 (200)	24	0.17 (349)	0.57	147	29.81		(511nm – 700nm)
7x7 Linear	0.10 (200)	48	0.17 (349)	$\sim$0.90	157	29.79		(511nm – 700nm)
Corner Designs								
5x5 Corner	0.03 (60)	8	0.63 (1293)	0.12	84	2.66	0.012*	(375nm – 700nm)
Radial Corner	0.03 (60)	26	0.41 (843)	0.33	46	4.07	0.023*	
5x5 Corner	0.04 (75)	8	0.62 (1261)	0.15	103	3.40	0.020*	(380nm – 700nm)
Radial Corner	0.04 (75)	21	0.41 (837)	0.34	57	5.12	0.036*	
5x5 Corner	0.05 (100)	8	0.59 (1208)	0.19	133	4.73		(390nm – 700nm)
Radial Corner	0.05 (100)	16	0.40 (826)	0.35	76	6.90		
5x5 Corner	0.10 (200)	8	0.49 (996)	0.37	231	11.35		(430nm – 700nm)
Radial Corner	0.10 (200)	8	0.38 (783)	0.37	144	14.32		
Special Cases								
Conical Linear	0.04 (75)	$\sim$298	0.20 (418)	0.48	5625	10.16	0.144	
Conical Linear	0.05 (100)	$\sim$377	0.20 (413)	0.47	10000	13.60	0.262	
Conical Linear	0.07 (150)	$\sim$534	0.20 (402)	0.44	22500	20.44		
Conical Linear	0.10 (200)	$\sim$691	0.19 (391)	0.42	40000	27.04		

Table 2. *Comparison of the CTIS designs.* D = (dim of the zero order) / (dim of the full array), N = number of projections, L = (pixels of spectral dispersion) / (dim of the full array). Values in parentheses are for an array of dimension 2048 pixels. The nonlinear designs have a Fourier cube scaled to $z = \pm 38$.

Design Parameters			Design Metrics					
Design Type	***D***	***N***	***L***	**Fill**	**Blur**	ϕ	γ	**Notes**
Nonlinear Designs								
3x3 Nonlinear	0.03 (60)	8	0.63 (1292)	0.16	43	2.66	0.012	
Spiral	0.03 (60)	16	1.16 (2372)	0.55	49	1.45	0.003*	
Radial Nonlinear	0.03 (60)	16	0.39 (807)	0.20	47	4.25	0.025	
3x3 Nonlinear	0.04 (75)	8	0.62 (1261)	0.20	53	3.40	0.020	
Spiral	0.04 (75)	16	0.96 (1970)	0.58	60	2.18	0.007*	
Radial Nonlinear	0.04 (75)	16	0.37 (762)	0.24	58	5.62	0.044	
Spiral	0.04 (75)	24	0.62 (1272)	0.57	58	3.40	0.016*	
Radial Nonlinear	0.04 (75)	24	0.32 (653)	0.31	56	6.55	0.075	
3x3 Nonlinear	0.05 (100)	8	0.59 (1208)	0.27	69	4.73	0.039	
Spiral	0.05 (100)	16	0.73 (1501)	0.60	79	3.87	0.021*	
Radial Nonlinear	0.05 (100)	16	0.33 (685)	0.29	74	8.30	0.096	
Spiral	0.05 (100)	24	0.45 (907)	0.57	75	6.29	0.055*	
Radial Nonlinear	0.05 (100)	24	0.27 (545)	0.36	71	10.38	0.191	
3x3 Nonlinear	0.07 (150)	8	0.54 (1102)	0.38	98	7.75		
Spiral	0.07 (150)	16	0.46 (934)	0.61	110	9.24		
Radial Nonlinear	0.07 (150)	16	0.26 (533)	0.38	101	15.70		
Spiral	0.07 (150)	24	0.22 (445)	0.49	96	19.02		
Radial Nonlinear	0.07 (150)	24	0.16 (329)	0.39	90	24.48		
3x3 Nonlinear	0.10 (200)	8	0.49 (995)	0.49	124	11.35		
Spiral	0.10 (200)	16	0.27 (555)	0.55	107	19.79		
Radial Nonlinear	0.10 (200)	16	0.19 (380)	0.42	148	27.70		
Special Cases								
Conical Nonlinear	0.03 (60)	$\sim$251	0.45 (914)	0.77	3600	3.76	0.019	
Conical Nonlinear	0.04 (75)	$\sim$298	0.44 (892)	0.77	5625	4.81	0.032	
Conical Nonlinear	0.05 (100)	$\sim$377	0.42 (854)	0.77	10000	6.68	0.061	
Conical Nonlinear	0.07 (150)	$\sim$534	0.38 (779)	0.76	22500	10.90		
Spiral	(10)	2	65.9 (135,000)					(nonimaging)

7. THE FOURIER REPRESENTATION OF CTIS DESIGNS

From the analogy of the CTIS measurement technique (measuring a 3D object, the datacube, from its 2D projections), we can make use of an important mathematical theorem that has found use in the computed tomography literature: the Fourier Slice Theorem. This theorem states that the Fourier Transform of a single projection (a 2D object) is equivalent to the Fourier Transform of the original object (in 3D) evaluated along a plane which passes through the origin. Thus, each footprint for a given CTIS design corresponds to sampling the Fourier cube (the Fourier Transform of the object's datacube) along a single plane. The effect of having many different projections is to sample along a number of planes tilted at different angles, but all of which pass through the origin in Fourier space.

There is a distinguishing feature to every CTIS design: a cone-shaped region, centered on the reciprocal-wavelength axis h, where none of the frequencies of the Fourier cube are sampled. This is a well-known problem for limited-angle tomography, and one which can cause considerably difficulty for accurate reconstruction. This provides another important characterization of the various CTIS designs: the size of the missing cone. In each of the Fourier representations, the geometry of the sampling planes allows us to obtain the missing cone angle, represented by ϕ, and the fraction γ of the Fourier cube which lies inside the cone.

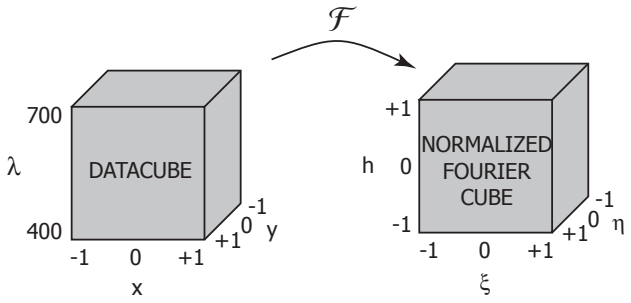

Figure 37. The nomenclature used for the axes in forward and reciprocal space.

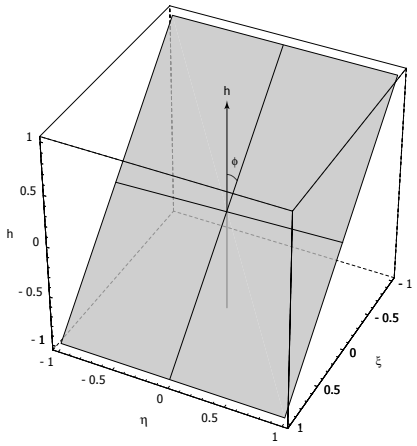

Figure 38. A plane in normalized Fourier space, tilted at angles of $\theta = 90°$, $\phi = 45°$.

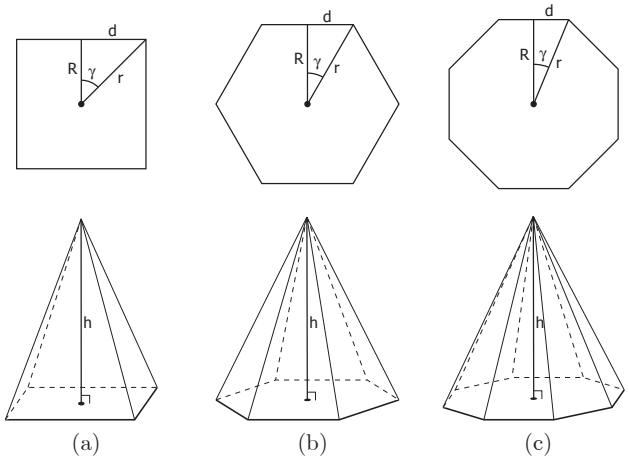

Figure 39. The shapes of the missing cone regions for (a) the 5×5 design CTIS (which has a square base), (b) a radial 6-projection design (the original Descour CTIS design), and (c) a radial 8-projection design.

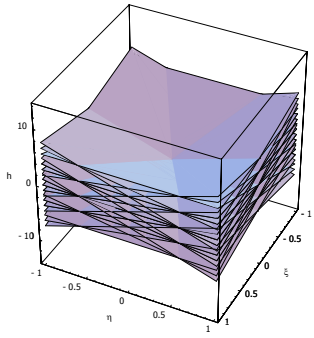

Figure 40. Descour design, $D = 100$, $N = 16$, $L = 550$.

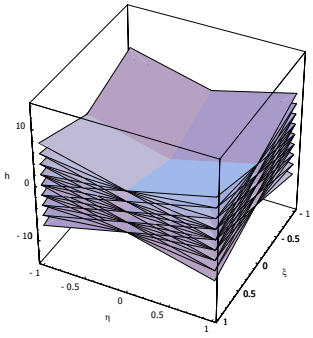

Figure 41. 5×5 design, $D = 100$, $N = 24$, $L = 526$.

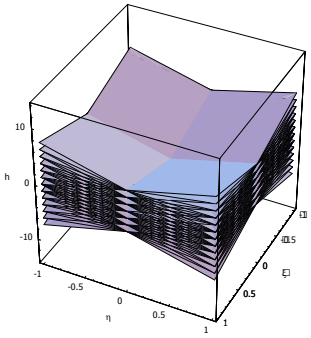

Figure 42. 7×7 design, $D = 100$, $N = 48$, $L = 526$.

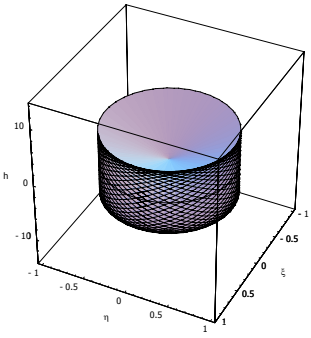

Figure 43. Linear radial design, $D = 75$, $N = 40$, $L = 419$.

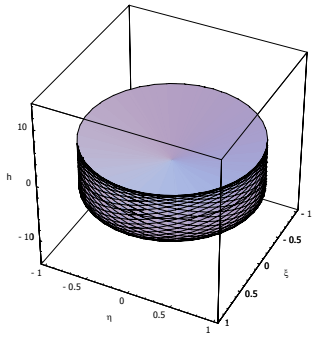

Figure 44. Linear radial design, $D = 100$, $N = 30$, $L = 413$.

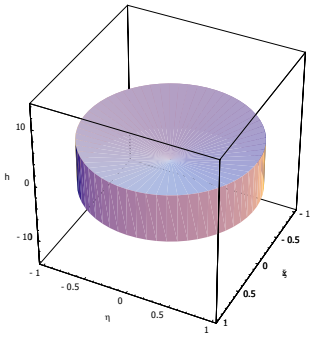

Figure 45. Linear conical design, $D = 100$, $N = \infty$, $L = 413$.

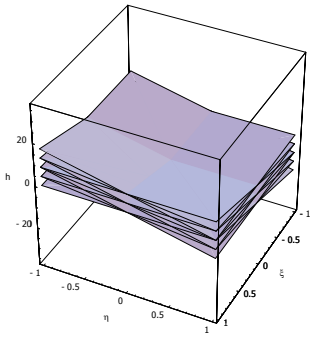

Figure 46. 5×5 corner design, $D = 100$, $N = 8$, $L = 1208$.

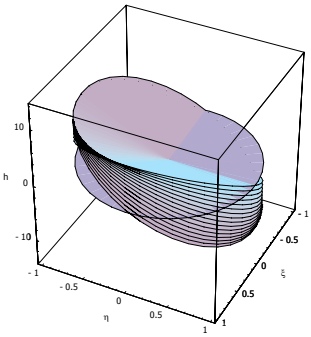

Figure 47. Linear radial corner design, $D = 100$, $N = 16$, $L = 826$.

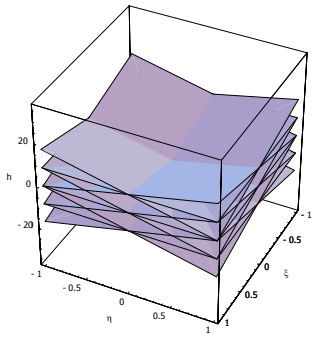

Figure 48. Nonlinear 3×3 design, $D = 100$, $N = 8$, $L = 1208$.

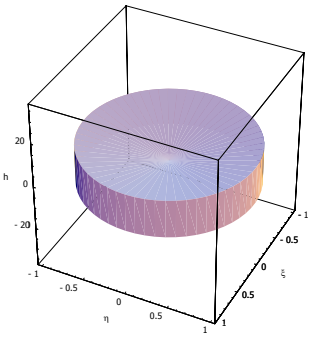

Figure 49. Nonlinear conical design, $D = 100$, $N = \infty$, $L = 854$.

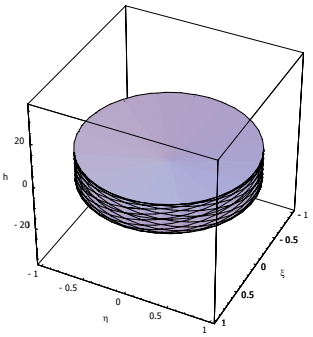

Figure 50. Nonlinear radial design, $D = 100$, $N = 16$, $L = 685$.

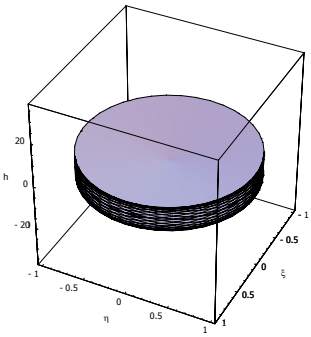

Figure 51. Nonlinear radial design, $D = 100$, $N = 24$, $L = 545$.

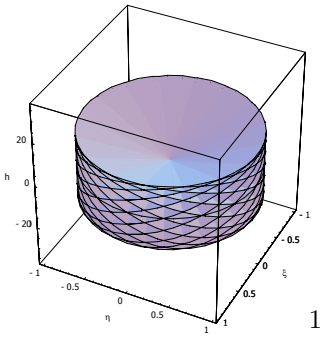

Figure 52. Spiral design, $D = 100$, $N = 16$, $L = 1501$.

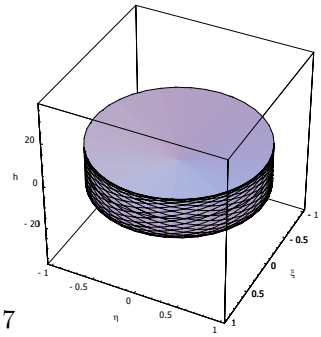

Figure 53. Spiral design, $D = 100$, $N = 24$, $L = 907$.

8. DESIGNING THE DISPERSER FOR THE NEW CTIS PATTERNS

After treating ideas relating to various CTIS design patterns, we have yet to consider how each design could possibly by manufactured for use in a real instrument. For past CTIS designs, all of which used "linear" gratings (for which the dispersion angle is linearly related to the wavelength), the technique for designing the dispersers has been a variant of the well-known Gerchberg-Saxton approach (also known as phase retrieval). This technique allows us to determine the phase profile of the grating which is capable of producing the desired intensity pattern on the focal plane array. For example, if we wish to construct a 5×5 CTIS pattern, then we can start by building the 25 dots onto a 2048×2048 data array. These represent the desired intensity pattern. Since we don't know the phase pattern on the array, we can just start by allowing all of the pixels to have random phase values. If we then take the inverse Fourier Transform of this function, then we have its Fourier representation at the pupil plane, where we intend to place the disperser. The disperser itself will be a transmission grating, and the light exiting the grating (if we limit ourselves to considering only monochromatic light for the moment) can be modelled as a plane wave multiplied by the phase function of the grating. That is, the physical model requires that we have a uniform amplitude at the pupil plane. The Fourier representation of the desired intensity pattern will almost certainly not have a uniform amplitude, and so we can keep the phase portion and replace the amplitude with a uniform value. Taking the forward Fourier Transform of the result, we have an approximation to the desired intensity pattern. It we continue to iterate this process, we can continue to refine the estimate so that the phases at the pupil plane accurately reproduce the desired intensity pattern at the focal plane (the diagram below illustrates this).

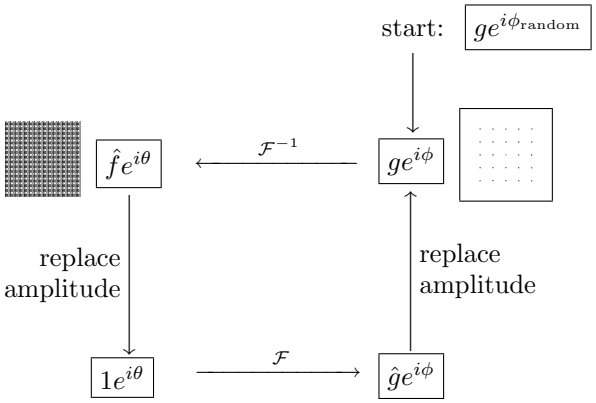

Using this technique, we can obtain the CGH designs for the 5×5 CTIS design, the Linear radial design, and the Linear conical design, as shown in Figures 54, 55, and 56. (In the greyscale phase maps, white corresponds to phase values of 2π and black to phase values of 0.)

For the *nonlinear* CTIS patterns, the disperser design approach is completely different. We are currently investigating whether we can make use of *volume* holograms in order to gain the added degrees of freedom to make a nonlinear disperser design. The basic idea is that we should be able to generate inside a holographic medium a set of multiple fringe fields, each one of which can be used independently to control the diffraction wavelength and diffraction angle of the input beam. Superimposing all of these fringe fields (a technique which has been mastered by holographic data storage researchers) should allow us to construct a complete diffraction pattern of almost any desired shape.

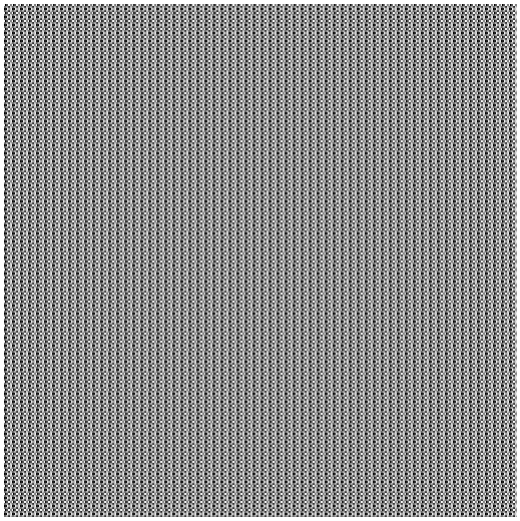

Figure 54. Greyscale map of the CGH pixel phases for the 5×5 CTIS design.

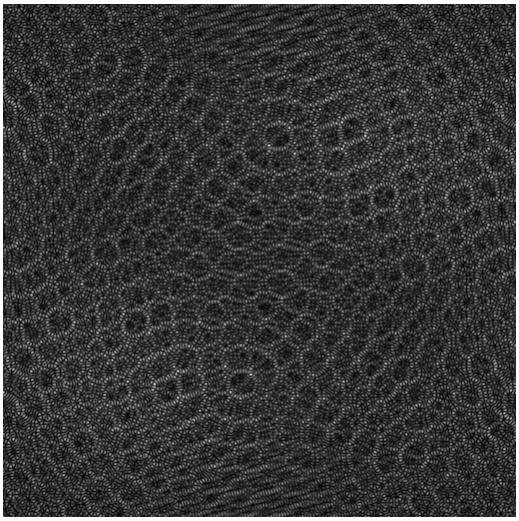

Figure 55. Greyscale map of the CGH pixel phases for the Linear radial CTIS design.

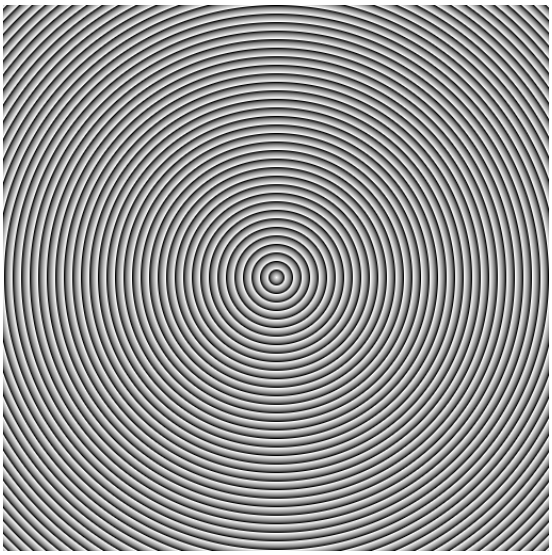

Figure 56. Greyscale map of the CGH pixel phases for the Linear conical CTIS design.

9. CONCLUSION

There still remain a number of barriers to practical implementation of the CTIS (and CTICS) instrument for remote sensing measurements. By attempting to integrate polarimetry into a CTIS instrument, one of these barriers — spectral resolution — becomes a particularly limiting factor. However, there are a number of paths promising large gains in CTIS capability. Altering the calibration method for CTIS has allowed us to construct an instrument capable of an order of magnitude better spectral resolution than previous CTIS instruments. Modifying the disperser design could further improve both spatial and spectral resolution by a factor of 2. If the nonlinear CTIS disperser designs prove to be workable, then an order of magnitude increase in spectral resolution becomes possible. Modifications to the reconstruction algorithms to improve their performance in the presence of noise may provide another factor of 2 to 4 in reconstruction data quality.

REFERENCES

1. T. Okamoto and I. Yamaguchi, "Simultaneous acquisition of spectral image information," *Opt. Lett.* **16**(16), pp. 1277–1279, 1991.
2. M. R. Descour, C. E. Volin, E. L. Dereniak, K. J. Thome, A. B. Schumacher, D. W. Wilson, and P. D. Maker, "Demonstration of a high-speed nonscanning imaging spectrometer," *Opt. Lett.* **22**(16), pp. 1271–1273, 1997.
3. M. R. Descour, C. E. Volin, E. L. Dereniak, T. M. Gleeson, M. F. Hopkins, D. W. Wilson, and P. D. Maker, "Demonstration of a computed-tomography imaging spectrometer using a computer-generated hologram disperser," *Applied Optics* **36**(16), pp. 3694–98, 1997.
4. C. E. Volin, M. R. Descour, and E. L. Dereniak, "Design of broadband-optimized computer-generated hologram dispersers for the computed-tomography imaging spectrometer," in Goldstein *et al.*,[9] pp. 377–387.
5. H. H. Barrett and K. Meyers, *Foundations of Image Science*, Wiley, New York, 2003.
6. K. Oka and T. Kato, "Spectroscopic polarimetry with a channeled spectrum," *Opt. Lett.* **24**(21), pp. 1475–1477, 1999.
7. K. Oka and T. Kato, "Static spectroscopic ellipsometer based on optical frequency-domain interferometry," in Goldstein *et al.*,[9] pp. 137–140.
8. D. S. Sabatke, *Snapshot spectropolarimetry.* PhD thesis, University of Arizona, Tucson, Arizona, 2002.
9. D. H. Goldstein, D. B. Chenault, W. G. Egan, and M. J. Duggin, eds., *Polarization Analysis, Measurement, and Remote Sensing IV*, *Proc. SPIE* **4481**, 2001.